Earth and Planetary Science Letters 271 (2008) 24–33

Contents lists available at ScienceDirect

Earth and Planetary Science Letters

journal homepage: www.elsevier.com/locate/epsl

Earth's core formation aided by flow channelling instabilities induced by iron diapirs

Gregor J. Golabek [a,b,*], Harro Schmeling [a], Paul J. Tackley [b]

[a] Department of Earth Sciences, Section Geophysics, Johann Wolfgang Goethe-University Frankfurt am Main, Altenhöferallee 1, D-60438 Frankfurt am Main, Germany
[b] Institute of Geophysics, ETH Zürich, Schafmattstrasse 30, CH-8093 Zurich, Switzerland

ARTICLE INFO

Article history:
Received 13 July 2007
Received in revised form 19 February 2008
Accepted 20 February 2008
Available online 6 March 2008

Editor: T. Spohn

Keywords:
core formation
planetesimals
Rayleigh–Taylor instability
differentiation
melt channelling
cascading mechanism

ABSTRACT

The core formation mechanism remains poorly known. An unstable gravitational configuration of a dense molten metallic layer overlying a cold chondritic protocore is predicted by most studies, which leads to the formation of a Rayleigh–Taylor (RT) instability. Recent results [Dahl, T.W., 2005. Turbulent mixing during planet accretion and core formation: Interpretation of the Hf/W chronometer and implications for the age of the Moon. M. Sc. Thesis, University of Copenhagen.] indicate that additionally, iron cores of predifferentiated planetesimals are also able to plunge mostly intact into the cold protocore and create large iron diapirs.
For both scenarios we propose the application of the stress-induced melt channelling mechanism [Stevenson, D.J., 1989. Spontaneous small-scale melt segregation in partial melts undergoing deformation. Geophys. Res. Lett. 16, 1,067–1,070] in the region surrounding an incipient iron diapir. We therefore perform numerical experiments solving the two-phase, two composition flow equations within a 2D rectangular box with symmetrical boundary conditions. We apply the Compaction Boussinesq Approximation (CBA) and include a depth-dependent gravity. For simplicity we use a constant viscosity for the solid phase and a melt fraction dependent rheology for the partially molten region around the diapir. We investigate the physical conditions under which the melt channels can form and whether they are applicable to the early Earth. As a result, for sufficiently small melt retention numbers iron-rich melt channels develop within a region of approximately twice the diapir's size. This could lead to effective draining of the surrounding region and might initiate cascading daughter diapirs. The region of the protocore drained by this cascading mechanism is expected to significantly increase with depth, and thus indicates an effective mechanism to also extract iron melt from deeper parts of the initially chondritic protocore. This mechanism could effectively accelerate the process of core formation.

1. Introduction

While the existence of the Earth's core is well established, the mechanism of its formation in the early history of the Earth is an unresolved question until now. The main unresolved dynamic problem is how the molten iron moved from the iron ponds down to the centre of the Earth, thereby passing through the ~3000 km thick protocore (Rubie et al., 2007). Elsasser (1963) proposed a series of catastrophic Rayleigh–Taylor (RT) instabilities which displace a cold protocore. During this overturn process stresses become very large and fracture or deform the protocore material so that it spreads as a mantle around the newly formed core (Stevenson, 1981). Following this idea numerical work performed by Honda et al. (1993) and recent results by Lin et al. (in preparation) showed that depending on the viscosity and therefore also the temperature of the protocore it is possible to switch from the above mentioned overturn mechanism in a cold interior to a regime where the Earth's core is formed by the sinking of many iron diapirs. Thus, the thermal history of the protocore plays an important role for the rheological precondition of core formation.

Current understanding (e.g. Chambers, 2004) indicates that accretion and differentiation of larger terrestrial bodies took place simultaneously. Two sources have been proposed to deliver the required energy for significant melting in the protoearth: decay of short-lived radioactive isotopes such as ^{26}Al ($t_{1/2}$=0.73 Ma) and the less prominent ^{60}Fe ($t_{1/2}$=1.5 Ma) (Carlson and Lugmair, 2000) and impact heating by accreted planetesimals (Melosh, 1990). Numerical models performed by Merk et al. (2002) show that an accreting planetesimal with about 100 km radius that is heated by the radioactive decay of ^{26}Al, can reach high central temperatures. Depending on the concentration of the isotopes, values between 600 and over 2000 K have been proposed in the case of homogeneous accretion. Thus, it would be possible to partially melt the iron in the protocore of a Mars-sized body and predifferentiate smaller bodies. Additionally, models of planetary formation indicate that the size of the impacting planetesimals increased with accretion time (e.g. Wetherill, 1990). Thus, at a certain point, a sufficient amount of impact energy was converted into heat to allow the formation of melt at or near the surface of the growing protoearth. Melosh (1990)

* Corresponding author. Institute of Geophysics, Schafmattstrasse 30, ETH Zürich, CH-8093 Zurich, Switzerland. Tel.: +41 44 633 3248; fax: +41 44 633 1065.
E-mail addresses: gregor.golabek@erdw.ethz.ch (G.J. Golabek), schmeling@geophysik.uni-frankfurt.de (H. Schmeling), ptackley@ethz.ch (P.J. Tackley).

0012-821X/$ – see front matter © 2008 Elsevier B.V. All rights reserved.
doi:10.1016/j.epsl.2008.02.033

suggested that this stage is reached when a planetary embryo equals at least 3600–3800 km radius (slightly larger than Mars size). This size can be reached after 0.1–10 Ma accretion time (e.g. Wetherill, 1990; Chambers, 2004), assuming a runaway growth of the planetary embryos. This is well within the lifetime of ^{26}Al and thus the combined effects could allow temperatures above the solidus of iron in some parts of the primordial protocore.

This leads to the scenario in which core formation started from an early impact generated magma ocean overlying a central undifferentiated protocore (see Stevenson, 1981, 1990; Karato and Murthy, 1997a). The magma ocean consisted of molten chondritic material, i.e. a homogeneous mixture of molten silicates and pure iron. Then two possibilities for diapir formation arise: Firstly, by the 'rainfall' mechanism (Stevenson, 1990; Rubie et al., 2003; Höink et al., 2006) gravitational separation of silicate and iron took place and ponds of molten iron accumulated at the base of this ocean. The lateral extent of these iron ponds depends on the viscosity of the uppermost layer of the central protocore: A relative thick iron layer (and resulting diapirs) may have formed at the base of the magma ocean as a result of many smaller, low energetic impacts, which can be expected shortly after melting is possible on the protoearth. Secondly, with proceeding accretion history iron cores of larger predifferentiated impactors (Taylor and Norman, 1990) could have plunged intact through the magma ocean as was shown by Dahl (2005), and could have generated large diapirs in the protocore. Ziethe and Spohn (2007) show that in case of temperature-dependent rheology iron diapirs sink with a velocity about a factor 30 higher than the Stokes sinking velocity in a isoviscous medium and may contribute to core formation within a reasonable time. But how does the pure iron (more than 20 wt.% of chondritic material) within the protoearth separate from the silicates? This question requires the consideration of melts in the protocore and is closely related to the mobility of a molten iron phase within the partially molten regions of the protocore. The mechanism of melt migration through the matrix depends on the wetting angle between the molten phase and the solid matrix. Under hydrostatic pressure, experiments on the system FeS and solid silicates show high wetting angles, prohibiting melt migration (Rushmer et al., 2000). Only at very high pressures (p=47 GPa) and temperatures (T=3000 K) (Takafuji et al., 2004) or very high S and O contents of the metal (Terasaki et al., 2007b) are dihedral angles reduced and melt interconnection may be possible. The conditions of the high p–T-experiments can be expected to be applicable only during the final phase of Earth's accretion. The high S and O contents as in latter experiments seem to be unlikely in the accreting Earth (Rubie et al., 2007).

Recent experiments indicate that the wetting angle may also be reduced by deviatoric stresses (Rushmer et al., 2000; Groebner and Kohlstedt, 2006; Hustoft and Kohlstedt, 2006). Once melt migration within a deviatoric stress field is possible, porous flow dynamics within a deformable matrix predict a channelling instability (Stevenson, 1989; Richardson, 1998; Katz et al., 2006; Müller and Schmeling, in revision). The time scale of this instability depends on the effective rheology of the porous matrix, which is not well known for real materials. Estimates based on analytical growth rates and numerical models predict that channel formation can be very fast: finite total strains as small as 10% might be sufficient to form well established melt channels (Stevenson, 1989; Müller and Schmeling, in revision).

Based on these ingredients we propose a new mechanism. In this conceptual model, the possible starting situations are depending on the temperature of the protocore and a global or regional magma ocean with a molten Fe/Ni pond at the base on a protoearth that is just massive enough to allow melting. Immediately beneath this layer the chondritic protocore is in a partially molten state. With depth and decreasing temperature the diverse silicate components of the magma ocean (Solomatov and Stevenson, 1993c) reach their solidus. Deeper beneath the upper boundary of the protocore, which is defined by the peridotite liquidus (Rubie et al., 2003), lies the remaining solid silicate matrix with molten Fe/Ni inclusions. Due to impact related perturbations RT instabilities may develop leading to starting iron diapirs sinking into the warmer upper part of the protocore. Depending on the rheological state of the upper boundary of the protocore, diapirs with different radii will develop. Additionally, intact impactor cores can plunge through the magma ocean and directly form iron diapirs within the protocore as shown by Dahl (2005).

For both scenarios of diapir formation the following development will be the same: Within a radius of approximately double to three times the size of the iron diapir, deviatoric stresses are sufficiently high to form an interconnected system of Fe/Ni-melt. Within this layer surrounding the initial diapir (let us use call this region '3-r_0-vicinity', where r_0 is the radius of the starting diapir) melt channelling occurs in response to the deviatoric stress field. Melt migrates along these channels down to regions where the initial stress field is too small to form an interconnected network of Fe/Ni. This is the region where the molten iron originating in the protocore material may accumulate. Eventually all iron within the 3-r_0-vicinity of the initial diapir accumulates at the base of this region, giving rise to a daughter iron diapir of radius r_1. In a sequence of cascading events these daughter diapirs sink down towards the centre of the Earth, each daughter diapir of radius r_i draining a cross sectional region of approximately 3-r_i radius. Depending on the growth rates of the channelling instabilities this mechanism can be much faster than the Stokes flow type of diapiric core formation, and is able to drain large regions of chondritic protoearth material. In the subsequent sections we quantitatively develop this conceptual model and quantitatively test its feasibility.

2. Model approach

2.1. Governing equations

The equations of conservation of mass, momentum and energy of a two-phase material consisting of fluid (subscript f, here molten iron) and solid matrix (subscript s) are given in the high Prandtl number approximation (McKenzie, 1984; Schmeling, 2000), but see also Ricard et al. (2001), who presented an alternative formulation relating compaction to an effective pressure difference between melt and solid.

$$\rho_f\left(\frac{\partial \phi}{\partial t}+\vec{\nabla}\cdot\left(\phi\,\vec{v}_f\right)\right)=0 \tag{1}$$

$$\rho_s\left(\frac{\partial (1-\phi)}{\partial t}+\vec{\nabla}\cdot\left((1-\phi)\,\vec{v}_s\right)\right)=0 \tag{2}$$

$$\vec{v}_f-\vec{v}_s=-\frac{k_\phi}{\eta_f\phi}\left(\vec{\nabla}P+\rho_f g\delta_{i3}\right) \tag{3}$$

$$-\rho g\delta_{i3}-\vec{\nabla}P+\frac{\partial \tau_{ij}}{\partial x_j}=0 \tag{4}$$

$$\frac{\partial C_m}{\partial t}+\vec{v}\cdot\vec{\nabla}C_m=0 \tag{5}$$

where ρ is the density, ϕ the porosity (equals the melt fraction), t the time, v the velocity, k_ϕ the permeability, η_f the melt viscosity, P the (fluid) pressure, g the gravity acceleration, δ_{ij} the unit matrix (Kronecker symbol), and τ_{ij} the deviatoric stress.

The last equation describes the advection of composition, C_m is the compositional field (either 0 or 1) describing the concentration of material m. The material m=1 denotes protocore material, m=2 represents molten iron diapir material.

The constitutive equations are

$$\tau_{ij} = \eta_s\left(\frac{\partial v_{si}}{\partial x_j} + \frac{\partial v_{sj}}{\partial x_i}\right) + \delta_{ij}\left(\eta_b - \frac{2}{3}\eta_s\right)\vec{\nabla}\cdot\vec{v} \tag{6}$$

$$k_\phi = k_0\phi^n \tag{7}$$

$$\rho = \rho_{Fe}\phi + (\rho_{Si}C_1 + \rho_{Fe}C_2)(1-\phi) \tag{8}$$

where η_b and η_s are the effective bulk and shear viscosities of the (porous) matrix, respectively, k_0 and n are constants of the permeability–porosity relation, ρ_{Fe} and ρ_{Si} are the densities of liquid iron or solid silicate, respectively.

The compaction Boussinesq approximation (CBA) is used (see Schmeling, 2000), which essentially neglects density variations except for the buoyancy terms. It also neglects compaction for the matrix flow, but accounts for compaction stresses and compaction pressure for the melt flow. This approximation is reasonable as long the melt fraction is smaller than 20% (see also Schmeling, 2000). The resulting flow equations for incompressible materials in two dimensions are

$$\left(\frac{\partial^2}{\partial x^2} - \frac{\partial^2}{\partial z^2}\right)\eta_s\left(\frac{\partial^2\Psi}{\partial x^2} - \frac{\partial^2\Psi}{\partial z^2}\right) + 4\frac{\partial^2}{\partial x\partial z}\eta_s\frac{\partial^2\Psi}{\partial x\partial z} = g\frac{\partial\rho}{\partial x} \tag{9}$$

where Ψ is the stream function, defined by

$$v_x^d = \frac{\partial\Psi}{\partial z}, \quad v_z^d = -\frac{\partial\Psi}{\partial x} \tag{10}$$

where $\vec{v}^d$ is the divergence free part of the matrix velocity.

The CBA has been tested by Schmeling (2000) and Müller (2005), who showed that the wavelength-dependent analytical growth rates of the melt channelling instability (Stevenson, 1989) could always be reproduced to better than within a few %. Other tests of the code, including a comparison of velocities of analytical and numerical solitary porosity waves, have been carried out by Schmeling (2000) and show excellent agreement. Therefore we are confident that the channel-like features developing as a consequence of the stress field of the diapir (see below) are well resolved.

For sake of simplicity, as we are mostly interested in the behaviour of the protocore region around the iron diapir, the viscosities of the diapir and the protocore have been assumed to be equal. Thus, any flow structures developing within the iron diapir have to be disregarded. In the partial molten protocore region the viscosity is assumed as only dependent on the melt porosity following an empirical law

$$\eta_s = \eta_0\exp(-a_1\phi) \tag{11}$$

where a_1 is a constant in the range 26–45 and η_0 is the viscosity of the melt-free protocore.

In our models we use a value of $a_1=28$, typical for partial molten peridotite (Kohlstedt et al., 2000). As has been discussed by Müller and Schmeling (in revision), this parameter a_1 controls the growth rate of the melt channelling instability at small wavelength. At such wavelength, the above value ensures the development of channelling instabilities after only a few 10% of straining.

Due to the above mentioned limitations of the CBA, the melt porosity cannot be allowed to increase to arbitrary values. Above a truncation value of 20% further increase of melt porosity had to be inhibited artificially in the models.

Thus, modelled melt channels with 20% melt are expected to evolve to even stronger localization and higher porosities (up to 100%) in nature and melt segregation would be significantly faster.

An important non-dimensional number of our problem is the melt retention number Rt (Tackley and Stevenson, 1993)

$$\mathrm{Rt} = \frac{\eta_f h^2}{\eta_0 k_0} = \frac{\eta_f h^2 b}{\eta_0 a^2} \tag{12}$$

where h is the height of the model in our setup, $k_0=a^2/b$ is the permeability pre-factor (see Eq. (7)), a is here the grain size whereas b is a geometrical factor ranging from 100 to 3000. For isotropically oriented fully connected melt tubules with equal circular cross sections b is 72π, while in the applied case of isotropically oriented fully connected melt films b is equal to 648 (Schmeling, 2000).

Rt scales with the ratio of the Stokes velocity of the diapir, v_{dia}, to the Darcy velocity of the percolating melt, v_{dar}, and can be written as:

$$\mathrm{Rt} = \frac{v_{dia}}{v_{dar}}\frac{h^2}{r_{Fe}^2}\phi^{n-1} \tag{13}$$

where r_{Fe} is the radius of the diapir. Hence, in the absence of melt channels and for melt porosities ϕ of the order of 0.1, $n=3$, and diapir radii between 25 and 200 km, retention numbers less than 6 to 0.1 are needed, respectively, to induce percolation velocities which are higher than the velocity of the sinking diapir. But in the following models we will see that even for Rt larger than the above mentioned values segregation velocities might be larger than diapir velocities via the mechanism of melt channelling instability.

2.2. Model setup and numerical scheme

To quantitatively test the conceptual model introduced in Section 1, our model set up is designed to describe a well developed starting diapir shortly after it has formed from an iron pond at the base of the magma ocean or by the impact of a predifferentiated planetesimal (see also Fig. 1). This allows us to neglect the effect of the magma ocean, and to focus on the effect of the diapir on the surrounding partially molten protocore. The diapir is introduced into the model as an initial condition as a circular region with $C_2=1$ and $C_1=0$ (i.e. with a density of $\rho=\rho_{Fe}$) embedded in a protocore region with $C_2=0$ and $C_1=1$ (i.e. with a density of $\rho=\phi\ \rho_{Fe}+(1-\phi)\rho_{Si}$). Diapir radii will strongly depend on whether they form from the iron layer (small) or impactor cores (large). Additionally the diapir radii can vary during runaway accretion due to the growth of the impactor size. As an indicator of possible diapir radii we may take the core size of the early formed asteroid 4 Vesta of 98–123 km (Ghosh and McSween, 1998). Application of the estimations of Vesta's mass ($M_{Vesta}=(2.75\pm0.24)\cdot10^{20}$ kg) compiled by Ghosh and McSween (1998) and Mars mass ($M_{Mars}=6.42\cdot10^{23}$ kg) (Lodders and Fegley, 1998) on results by Ziethe et al. (in preparation), which suggest that the most probable mass ratio during accretion is $10^{-4}<M_1/M_2<10^{-3}$ between impactor mass (M_1) and mass of impacted body (M_2), gives good agreement for an Vesta-sized impactor on an Mars-sized protoplanet as used in our model. Thus we use the range from 25 to 200 km radius for our starting diapirs, which we can resolve reliably with our code. These should cover the range where at least one of the two diapir formation mechanisms may be active.

We performed models with two different settings. The first case assumes a quadratic box with 2000 by 2000 km, representing a significant part of the outer protocore, in order to exclude any interactions with any other diapirs. This scenario can be important shortly after the diapir begins sinking. The incipient diapir is always placed in the same initial position at a distance of at least one diapir radius (in the case of 200 km radius) away from the boundaries. The second setup represents the development in case of interaction with neighbouring diapirs as we use free slip on all boundaries of the numerical setup. This can be important for later stages of the sinking as will be explained below. The size of the model box was assumed as a rectangular region of 750 by 2000 km.

For the sake of simplicity the equations are solved in 2D Cartesian coordinates, neglecting spherical effects of the Earth or of a spherical diapir. Due to numerical restrictions the box is limited in size. This is a first step, and we believe that this simplification does not affect the principal behaviour of the core formation process we are interested in.

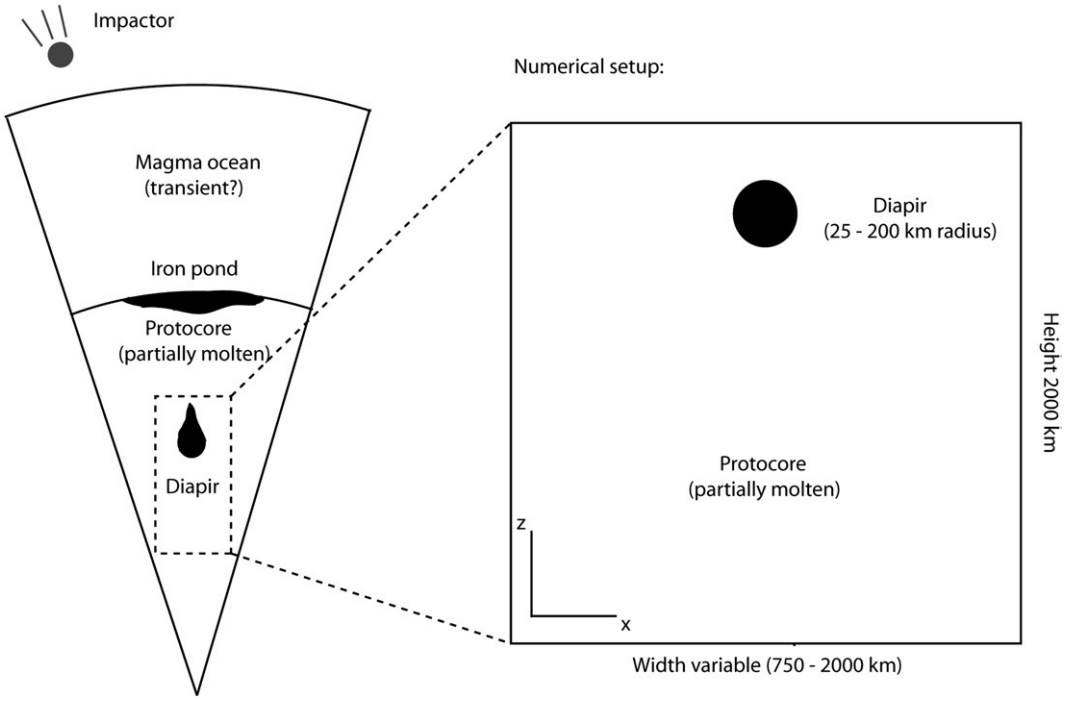

Fig. 1. Schematic diagram showing the basic idea of the theoretical cross section of the protoearth and the numerical setup used.

The study of spherical and 3D effects will be left to future work. For our model we assume a protoearth with $3.6 \cdot 10^6$ m radius, slightly larger than today's Mars. The gravitational acceleration is assumed to be linearly depth-dependent decreasing from 4.4 m s^{-2} at the top to 2.0 m s^{-2} at the bottom of the box. For simplicity we do not solve the energy equation, thus, implicitly we assume a temperature slightly below the peridotite solidus, but above the Fe-melting temperature. Initially the protocore region ($C_1 = 1$) has a molten iron content of 0.1, i.e. the porosity is assumed to be 10%. The addition of white noise on the porosity with an amplitude of ±0.005 permits the development of the melt channelling instability in the models. Generation of new melt and crystallization are not accounted for.

Experimental results show that the pinch-off value for FeS melt interconnectivity in a solid peridotite matrix may lie around 5 vol.% in static experiments (Yoshino et al., 2004). In the most abundant chondritic materials values between 18.5 wt.% (=8.5 vol.%) (LL chondrites) and 27 wt.% (=13.1 vol.%) (H chondrites) iron can be expected (Kallemeyn et al., 1989). Thus, protocore material is expected to be above the critical melt percentage allowing interconnectivity. Therefore in our model we assume an interconnected melt system.

The Eqs. (1)–(10) are solved by a combined finite difference (FD)-marker approach (Weinberg and Schmeling, 1992; Schmeling, 2000). Eq. (9) is written in FD, and solved directly by Cholesky decomposition and resubstitution. Eqs. (1)–(3) are solved iteratively for each time-step by FD using an upwind scheme. Eq. (5) is solved by a marker approach described by Weinberg and Schmeling (1992). We performed our models using a standard resolution of 216 by 216 for the first and 81 by 216 grid cells for the second case, whereas the porosity is calculated on a two or four times finer grid with 431 by 431 or 321 by 861 grid cells. To quantify our results we performed a resolution test on the first case applying basic resolutions ranging from 56 by 56 to 243 by 243 (see Fig. 2). It showed that using the before mentioned resolution, all important features were well resolved.

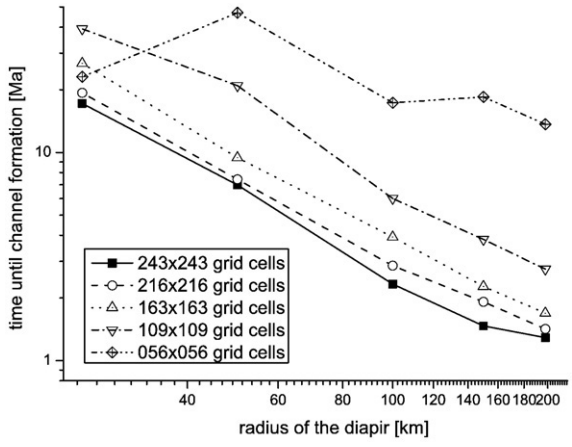

Fig. 2. Resolution test for different diapir radii. It confirms that for high resolutions the melt channelling instability develops also for smaller diapirs. The graphics also suggests that in 2D the development time of melt channels scales with r_i^{-1}.

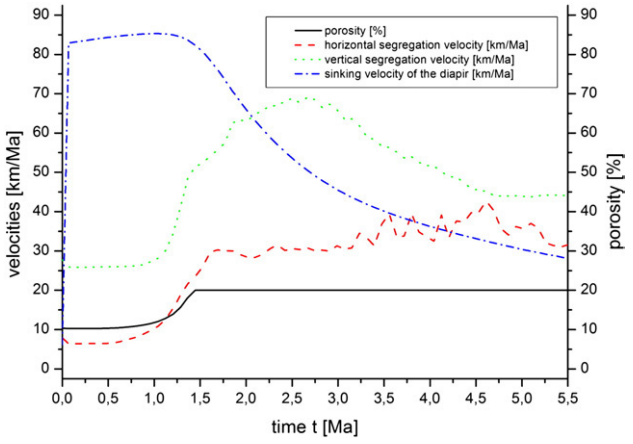

Fig. 3. Segregation and sinking velocities for a typical run using a diapir with $r = 1.98 \cdot 10^5$ m dependent on the porosity for Rt = 1.0. black: porosity in %, light grey: maximum vertical sinking velocity of the inducing diapir in km/Ma, grey: maximum horizontal segregation velocity of the iron melt in km/Ma., dark grey: maximum vertical segregation velocity of the iron melt in the channels in km/Ma.

3. Results

3.1. General behaviour of the channelling instability

As the porous flow behaviour of the iron-silicate bearing protocore is not well constrained, we varied the value of the Rt number in order to investigate the evolution of the melt within the protocore material surrounding the diapir. Fig. 3 shows the temporal behaviour of important quantities of a typical case 1 model with Rt = 1.0 (e.g., corresponding to $\eta_f = 3.86 \cdot 10^2$ Pa s, $h = 2.0 \cdot 10^6$ m, $b = 648$, $\eta_0 = 10^{24}$ Pa s, $a = 10^{-3}$ m). The velocity of the diapir during the first 1.2 Ma is around 85 km/Ma, which is a value similar the Stokes velocity for a sphere with 200 km radius in a medium with a reduced viscosity due to the presence of melt (see Eq. (11)). First it slowly increases with time due to decreasing influence of the upper boundary of the model. Starting with a rather homogeneous melt distribution, after about 1.4 Ma the small initial porosity fluctuations develop into channels with high melt concentrations and higher density, separated by regions of low melt concentrations and lower density. These are regions of low and high pressure, respectively; these pressure differences drive the channelling instability (Fig. 4). As a consequence of the viscous stress field around the diapir, the channels are essentially directed radially away from the diapir in the lower part, while they are subhorizontal behind the diapir.

As depicted in Fig. 4D for a diapir with 200 km radius, with increasing time the porosity increases, which is equivalent to the development of the melt channels. This behaviour is accompanied by a change of both the diapir velocity and the segregation velocity. While the diapir slows down, the horizontal and vertical segregation velocities strongly increase due to the increasing permeability of the medium. The results of this model indicate that the development of horizontal and vertical channels starting at 1.0 Ma is completed within 0.5 Ma, as seen by the much higher melt velocity in the later stages (see again Fig. 3). Similar behaviour as described above can be seen in the case of smaller diapirs (see Fig. 4A–C), where the general behaviour remains the same, but the timescale for channel development changes. We find that the time until channel formation increases proportional to $1/r_i$ (see Fig. 2). It should be mentioned that this is an

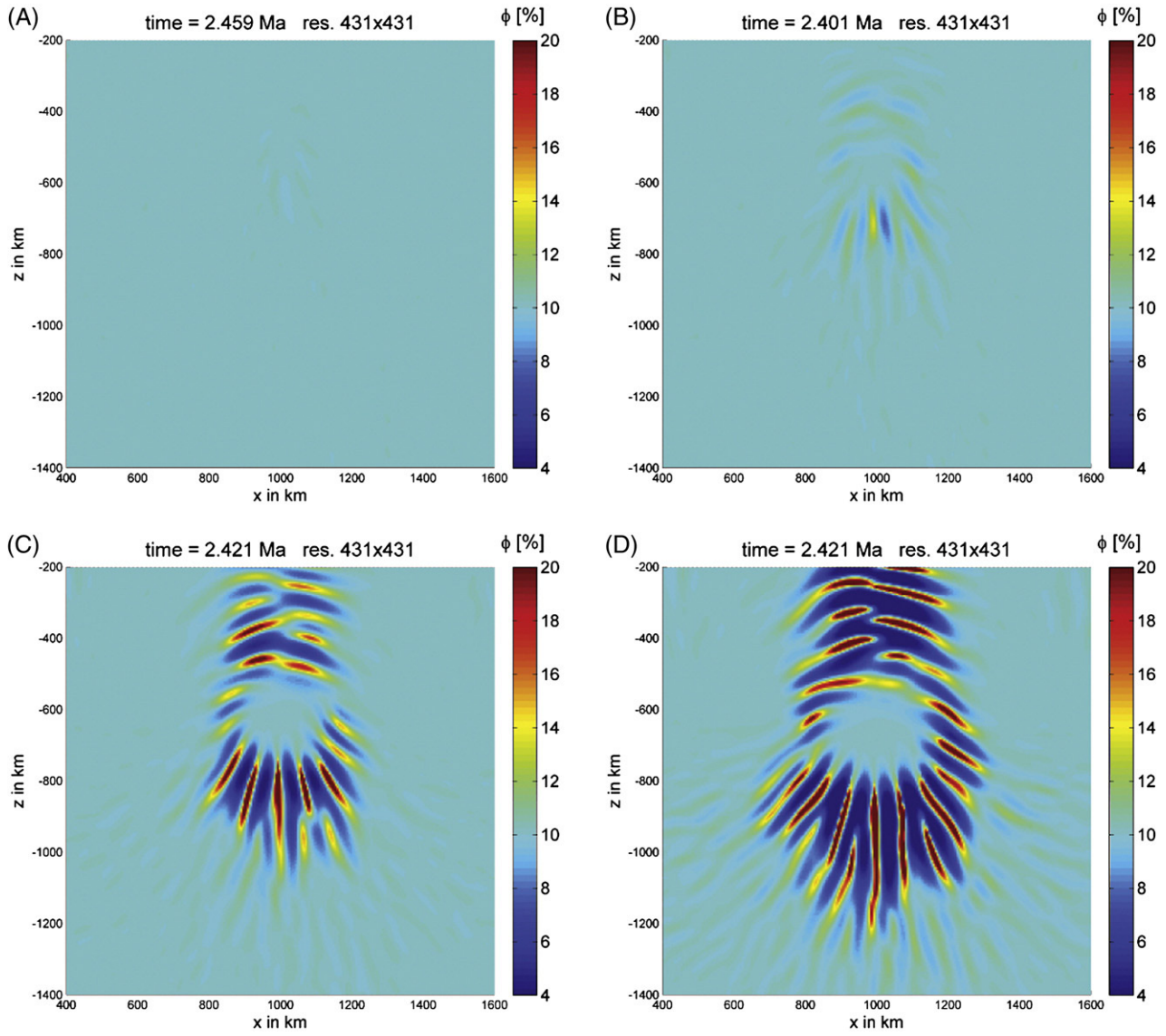

Fig. 4. Close-up view of the changing stage of development of the melt channels depending on the radius of the inducing diapir. Shown are the surrounding porosities for diapirs with different radii (A) 50 km, (B) 100 km, (C) 150 km and (D) 200 km for similar timesteps in the case of Rt = 1.0. Note that the depleted regions in (C) and (D) have even lower porosities than 4% in the depleted regions between the channels, but a common colorbar was used for all subfigures.

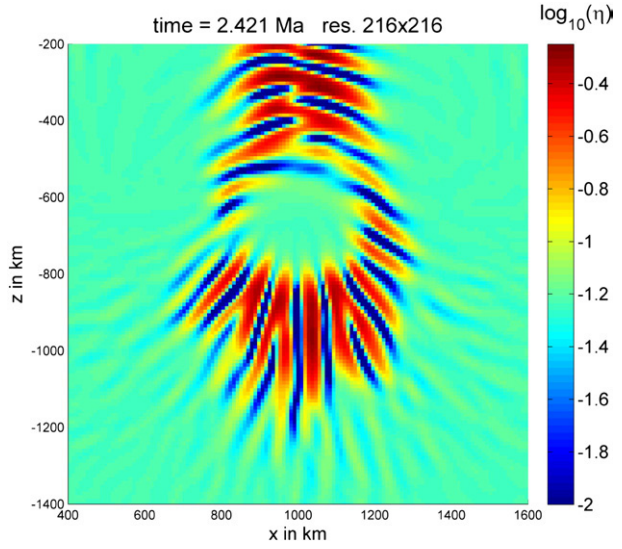

Fig. 5. Logarithm of the viscosity around the diapir due to melt channelling. The protocore viscosity is largely reduced by the existence of melt to values around $6{\cdot}10^{22}$ Pa s (see Eq. (11)), while the viscosity in the melt focussing channels is reduced further and increased in melt depleted regions.

effect of our two dimensional calculations as theoretical calculations in 3D indicate a $1/r_i^2$ dependency. Our numerical results show that for diapirs with at least 25 km radius, the instability will develop. This is confirmed by the results of the above mentioned resolution test (see again Fig. 2).

The formation of a well developed channel system and the subsequent rise of the segregation velocities have direct implications on the maximum sinking velocity of the diapir. It is reduced to less than 40% of the initial velocity at the end of the numerical run. In this case of developed melt channels we observe the formation of an effectively anisotropic viscosity distribution in the medium surrounding the sinking diapir (Fig. 5). Due to the radial distribution of the high–low viscosity channels, the effective viscosity 'seen' by the diapir is dominated by the high viscosity layers (effective viscosity = arithmetic mean of local viscosities). Furthermore, because of the high segregation velocities of the melt in the channels (Fig. 6A and B) the channels can effectively deplete the region below the diapir of iron melt. Therefore we see the development of a rheological drainage hardening in the region below the diapir. This leads to the drastic reduction of the sinking velocity of the diapir. The final velocity of the diapir will drop even further and will finally reach the Stokes velocity for a sphere sinking in the melt-free, highly viscous medium. After formation of a well developed channel system ($t > 2$ Ma for the model shown in Fig. 3) the melt velocity is about 1.2 to 1.6 times higher than the diapir velocity (Figs. 3 and 6).

The melt channels are limited to a 3-r_0-vicinity, which is equivalent to the region in which the deviatoric stress field surrounding the diapir is important (Fig. 7). The stress field is strongest mainly in the regions below (vertical compression) and above (horizontal compression) the diapir. This allows the preferred development of vertical melt channels in the high deviatoric stress region in front of the diapir (see also Fig. 4A–D) and the development of subhorizontal channels above the diapir. Vertical shear stresses at the sides of the diapir induce channels with about 45° inclination. Note that the stresses inside the diapir are unrealistic because of our limitations on the rheology in the diapir (see Section 2).

3.2. Models with smaller aspect ratio

In case 2 we apply a narrower numerical box, which can be important in the case of small wavelength from which nearby neighbouring diapirs would form. The development of the melt channelling instability in this case is limited to the vicinity of high deviatoric stresses surrounding the diapir (Fig. 7), which is about half the wavelength between the neighbouring diapirs. The branches in horizontal direction are much more developed than in the previous case and the stress field is less focussed on the regions below. The stress field exhibits two characteristic subhorizontal branches extending to the symmetric side boundaries, i.e. towards the positions of the virtual neighbouring diapirs. The orientation of the stress field within these branches promotes the evolution of subhorizontal melt channels. Thus, the preferred development of subhorizontal channels in front of the diapirs for small aspect ratio models such as those shown in Fig. 8 is a consequence of the use of the symmetrical boundary condition at both sides.

3.3. Model with varying Rt

For the case 1 setup and Rt > 25 (e.g. corresponding to $\eta_{lf} = 9.6 \cdot 10^3$ Pa s, $h = 2.0 \cdot 10^6$ m, $b = 648$, $\eta_{l0} = 10^{24}$ Pa s, $a = 10^{-3}$ m) melt percolation is slowed down and the development of melt channelling instabilities is completely suppressed. The segregation velocity field shows a dipolar flow field which is expected for a single sinking sphere (see as an example Fig. 9). High dynamic pressure in front of the diapir pushes the melt to the sides and then upwards towards the low-pressure wake of

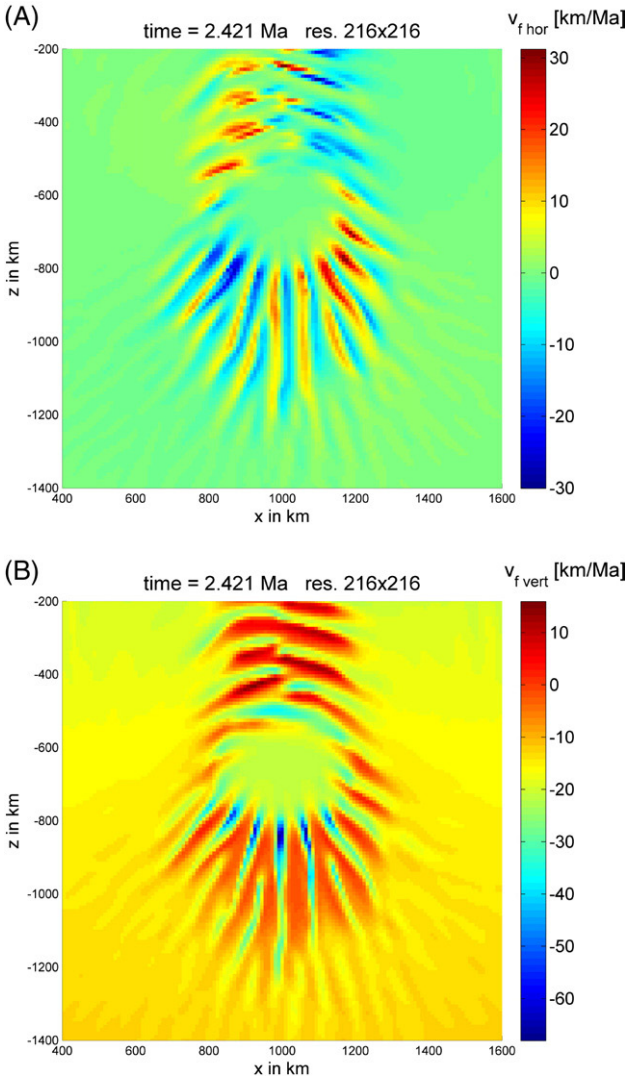

Fig. 6. Close-up view of (A) vertical and (B) horizontal segregation velocity of the region surrounding the diapir in km/Ma for Rt = 1.0. The regions of channel formation (high porosities) depicted in Fig. 4D and the regions showing high segregation velocities correlate with each other.

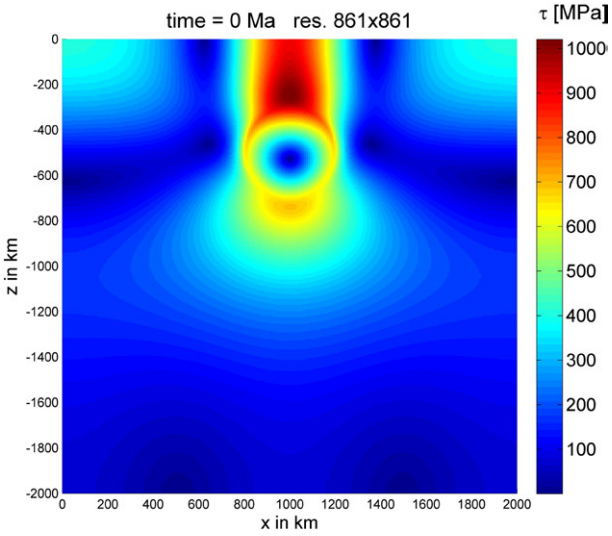

Fig. 7. Close-up of the deviatoric stress field of the diapir for case 1 (aspect ratio 1.0) using Rt = 1.0. Undisturbed diapirs show a stress field preferentially oriented in the vertical direction. In this high deviatoric stress region surrounding the sinking diapir we observe the development of iron melt channels.

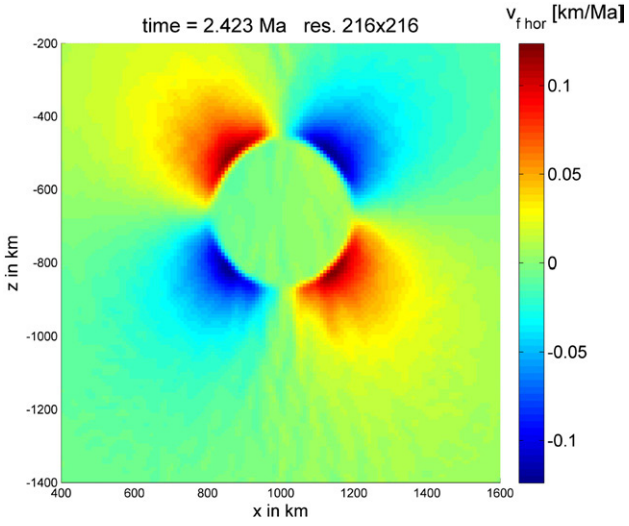

Fig. 9. Close-up of the horizontal segregation velocity in km/Ma using the aspect ratio of 1.0, but with Rt = 50.0 shown for a similar time as in Fig. 6A. As can be seen, melt channels are absent and the segregation velocities are more than two orders of magnitude lower than in the first case.

the diapir. For Rt numbers less than 25 melt percolation increases and our models show the development of melt channelling instabilities. The segregation velocity field in Fig. 6A and 6B (Rt = 1.0) is more than two orders of magnitude higher than in the previous case (Rt = 50), indicating that not only the Darcy velocity has increased inversely proportional to Rt, but additionally melt channels dominate the flow field. For Rt = 1 the melt in the channels migrates with a vertical segregation velocity 2.5 times faster than the melt diapir.

4. Discussion

4.1. Angles and wavelengths of the melt channels

In our models the melt channelling instability leads to channels oriented into the direction of maximum compressive stress in agreement with the results of Richardson (1998), Müller (2005) and Müller and Schmeling (in revision). As discussed by Müller and Schmeling (in revision) at later stages this direction may on average be rotated by as much as 10 to 20° into the direction of simple shear (i.e. 50–60° from the shear plane), indicating that a direction more or less parallel or subparallel to the maximum compressive stress may still be applicable. The formation of melt channels during deformation of solid–melt mixtures has also been observed by Groebner and Kohlstedt (2006) for the system olivine and gold. However, in contrast to the numerical results mentioned above, laboratory experiments observe orientations closer (13–15°) to the shear plane. While explanations of these differences are not yet conclusive (see e.g. the discussion by Groebner and Kohlstedt, 2006) and include microcracking as a possible mechanism influencing the orientation of melt bands, one has to be aware that the laboratory experiments have been carried out under high strain rate ($O(10^{-2}$–10^{-4} s^{-1})) and stress (O(100 MPa)) conditions, while the protocore models act on a low strain rate scale of 10^{-13}–10^{-14} s^{-1} and a comparable stress scale.

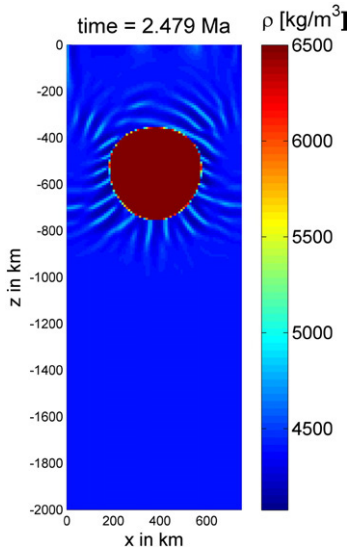

Fig. 8. Development of melt channels surrounding the inducing diapir for case 2 (aspect ratio 0.375) with Rt = 1.0 and a resolution of 81 times 216 grid cells. Shown is the density in the protocore. We apply a cut-off density for plotting purposes because of the much higher density of the diapir itself. We observe that in contrast to the case applying high aspect ratio, preferentially subhorizontal melt channels develop, which point to the virtual neighbouring diapirs. This indicates melt partition in the case of close-by diapirs.

Linear stability analysis of the melt channelling instability (Stevenson, 1989) indicates that there does not exist a characteristic wavelength corresponding to maximum growth rates. However, numerical experiments by Richardson (1998) and Müller and Schmeling (in revision) as well as the models shown here seem to predict a dominant wavelength of the melt channelling instability. As discussed in Müller and Schmeling (in revision) this observation may be due to the restrictions of numerical grid resolution. In this respect, an important quantity related to the growth rate of the melt instability is the compaction length (McKenzie, 1984)

$$\delta_c = \left(\frac{(\eta_b + \frac{4}{3}\eta_s)k_0}{\eta_f}\right)^{1/2} \cdot \phi^{n/2} \tag{14}$$

which can be written in terms of Rt

$$\delta_c = \frac{h}{Rt^{1/2}}\left(\frac{\eta_b + \frac{4}{3}\eta_s}{\eta_0}\right)^{1/2} \cdot \phi^{n/2}. \tag{15}$$

Thus, keeping the solid viscosity η_0, box height h and melt fraction ϕ the same at the onset of our models, varying Rt implies that the compaction length is different for models with different Rt. This is

Table 1
Values of the physical parameters in the protoearth

Parameter	Estimation	Computationally feasible	Ref.
Thickness protocore, R	$3.2{\cdot}10^6$ m	$3.6{\cdot}10^6$ m	(Melosh, 1990)
Radius iron diapir, r_{Fe}	(0.25–1.98)·10^5 m	(0.25–1.98)·10^5 m	
Viscosity, η_0	10^{18}–10^{28} Pa s	10^{24} Pa s	(Karato and Murthy, 1997a)
Melt viscosity, η_f	10^{-3}–10^{0} Pa s	10^{24} Pa s	(Rubie et al., 2003)
Initial porosity, ϕ	0.1	0.1	
Gravity acceleration top, g	4.4 ms^{-2}	4.4 ms^{-2}	
Gravity acceleration gradient, dg/dz	$1.2{\cdot}10^{-6}$ s^{-2}	$1.2{\cdot}10^{-6}$ s^{-2}	
Thermal diffusivity, κ	$1{\cdot}10^{-6}$ m^2 s^{-1}	$1{\cdot}10^{-6}$ m^2 s^{-1}	
Heat capacity, c_p	$1.3{\cdot}10^3$ J kg^{-1} K^{-1}	$1.3{\cdot}10^3$ J kg^{-1} K^{-1}	
Thermal expansivity, α	$1{\cdot}10^{-5}$ K^{-1}	$1{\cdot}10^{-5}$ K^{-1}	(Steinberger and Calderwood, 2006)
Solid density silicates, ρ_{Si}	4500 kg m^{-3}	4000 kg m^{-3}	(Ziethe and Spohn, 2007)
Melt density iron, ρ_{Fe}	7000 kg m^{-3}	8000 kg m^{-3}	(Ziethe and Spohn, 2007)
Grain size upper protocore, a	10^{-3}–10^{-2} m	10^{-3}–10^{-2} m	(Karato and Murthy, 1997a)
Geometrical factor, b	648	648	(Schmeling, 2000)

important as the linear stability analysis of the melt channelling instability predicts that only at wavelengths smaller than the compaction length melt channels may form sufficiently fast. For such wavelengths, the growth rates become independent of wavelength, implying the possible existence of channels with arbitrarily small wavelengths. Given a melt fraction of 0.1 the above equation implies that for Rt much larger than 1 the channel instability would still occur, but at wavelengths $\lambda << h$ which is beyond the resolution of our model (see Müller and Schmeling, in revision). Thus, even if we do not observe channelling instabilities in our models with large Rt, they are expected to occur with the same growth rate as for low Rt, but only at smaller wavelengths. For example in the case of Rt=25 the compaction length is only 0.2 times the compaction length for Rt=1. This can explain the absence of melt channels for Rt values higher than 25 in our models.

However, one has to be aware that realistic Rt numbers for the protocore with the dimensions h and viscosities η_0 from Table 1 of our model would be of the order of 10^{-10}–10^{-2} (given the uncertainties in k_0 and η_f). In other words, our applied Rt numbers would for example overestimate the melt viscosity, as can be seen in the example calculations in Sections 3.1 and 3.2. As our models show increasing strength of the channelling instability for decreasing Rt numbers, our proposed mechanism must be even more important for the realistic protoearth.

4.2. Formation of daughter diapirs and the cascading mechanism

The most important characteristics of our model results are the formation of melt channels within a high stress region of radius of $q \cdot r_i$ around the diapir of radius r_i. The subscript i indicates the i-th generation of the diapir. The value of q decreases from 3 in early stages of the sinking to about half the actual wavelength when diapir draining regions start to interact. Melt will be drained out of this region through channels and accumulate near the bottom of the drained region. For every mother diapir this accumulated melt may form a new, daughter diapir, which, if sufficiently large, will be able to produce another drainage region. This leads to the cascading model as depicted in Fig. 10A.

We now extend this cascading model to three dimensions, and estimate the volumes and depths of the subsequent daughter diapirs. We assume that the diapirs of the first generation have originally formed from RT instabilities or impacts with a certain wavelength at the base of the magma ocean. We suppose that the diapirs of the $(i-1)$-th generation already have drained a cylindrical or cone-like region above, and all this melt makes up the size of the individual diapirs, i.e. determines their radius r_{i-1}. These diapirs need to sink a small distance of about $p \cdot r_{i-1}$ to allow for the formation of sufficiently well developed channels within a spherical cap with radius $q \cdot r_{i-1}$ underlying the previously drained region. Finite strains of the order 0.3–0.4 are needed for channel formation. Thus p, the sinking depth to initiate melt channels scaled by the diapir radius, will also be of the order of 0.3 to 0.4. It should be noted that the value depends on the Rt number. All melt within this cap-like region plus the melt collection during the sinking distance $p \cdot r_{i-1}$ is assumed to accumulate at the base of the drained region. In addition, we assume that the melt channels surrounding the $(i-1)$-th diapirs provide a pathway, to allow perfect drainage of these diapirs into the new generation of daughter diapirs. Thus we can estimate the volume of these daughter diapirs. However, the diapir growth changes significantly, once the draining regions start to interact, thus the radius of the spherical cap $q \cdot r_{i-1}$ is less than half the wavelength $\lambda_i(z)/2$, the wavelength in a certain depth. We assume for simplicity a spherical shape. When deriving the following two equations for the early and later development stage a few geometric simplifications have been applied leading

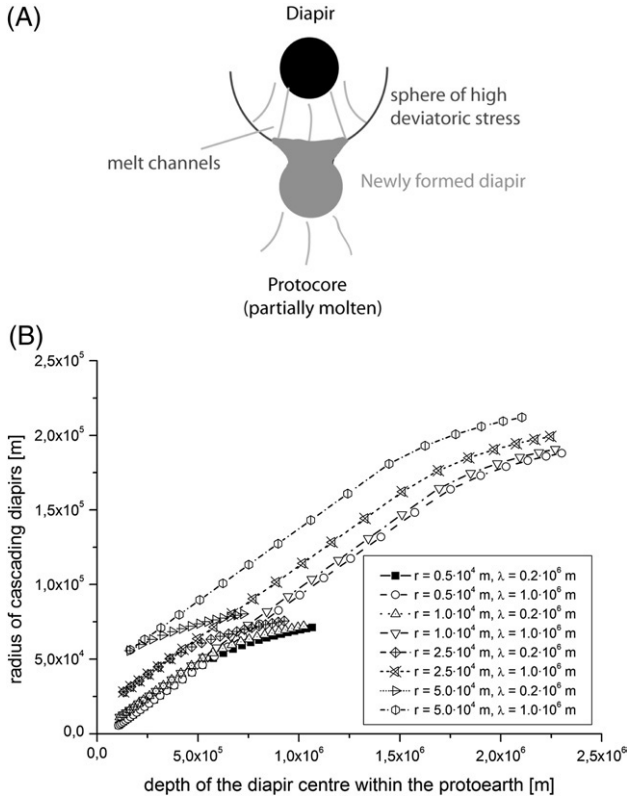

Fig. 10. (A) Collage of the possible cascading mechanism. (B) Speculative growth of diapirs with 5, 10, 25 and 50 km radius for starting wavelengths of 200 and 1000 km at the surface and a porosity ϕ of 10%. The starting depth is assumed to be 100 km. For larger wavelengths it takes longer until the diapir draining zones start to interact, so larger radii can be reached before the growth ceases. In the case without interaction the depth–radius relation would remain a straight line. The closer the diapirs are the narrower is the deviatoric stress field and the cascading events become more frequent with depth. The shown bended curves may underestimate the radius of the cascading diapirs as they are only valid in the special case, where the sinking diapir is surrounded by equidistant interacting diapirs. The curves halt, when the condition $r_i \geq \lambda_i(z)/2$ is fulfilled and merger processes start.

to an error of r_i of a few % at most. We get the following formulae for the radius of the interacting diapirs

$$r_i = \sqrt[3]{r_{i-1}^3 + \frac{3}{4}\phi\cdot\left(\frac{\lambda_{i-1}}{2}\right)^2\cdot\left[\frac{\lambda_{i-1}}{2} + r_{i-1}\cdot(p-1)\right]} \quad \text{For } q\cdot r_{i-1} \geq \lambda_{i-1}(z)/2. \tag{16}$$

In the case of absent overlapping of the draining zones, which is valid for the early stages of sinking, we find that the radius of this i-th diapir will be

$$r_i = r_{i-1}\cdot\left[1 + \frac{3}{4}\phi\cdot q^2\cdot(q-1+p)\right]^{1/3} \quad \text{For } q\cdot r_{i-1} < \lambda_{i-1}(z)/2. \tag{17}$$

The centre depth of the new diapir can be estimated for both cases to be at a distance r_i above the bottom of the newly drained region, i.e., at

$$z_i = z_{i-1} + \frac{\lambda_{i-1}}{2} + pr_{i-1} - r_i \qquad \textit{For } q\cdot r_{i-1} \geq \lambda_{i-1}(z)/2 \tag{18}$$

and

$$z_i = z_{i-1} + qr_{i-1} + p\cdot r_{i-1} - r_i \quad \text{For } q\cdot r_{i-1} < \lambda_{i-1}(z)/2 \tag{19}$$

where z_{i-1} is the centre of the $(i-1)$-th diapir.

Finally, we define the depth-dependent wavelength

$$\lambda_i(z) = \lambda_0\cdot(R - z_i)/R \tag{20}$$

where R is the radius of the protoearth. For derivations see online supplementary material.

The interaction between the diapirs tends to partition the available melt volume in the overlapping regions during drainage, as indicated by our models with small aspect ratio (see also Fig. 8). Thereby the increase of the individual diapir radius is inhibited. Using Eqs. (16)–(20) for starting diapirs of 5 to 50 km radius and ϕ of 0.1, the radii and depths of a series of cascading diapirs have been calculated, which are shown in Fig. 10B. For q we applied the more conservative value of 2 for interacting diapirs based on our model results. For the wavelength we used starting values of 200 and 1000 km. The size increases for subsequent generations of diapirs until the drainage regions start to interact. This growth is due to the drainage of iron melt from the chondritic protocore within a $q\cdot r_i$-vicinity of the i-th diapir, and increases also with the porosity of the surrounding medium as can be seen in Eqs. (16) and (17). As the volumes of the new diapirs increase, their sinking velocity increases proportional to r_i^2, thus the time scale for channel formation will be reduced significantly. This may lead to rapid core formation.

4.3. Required temperatures

Our model requires that a temperature above iron solidus must be ensured in the region surrounding the particular diapir. The question remains whether the temperatures can be kept high enough in lower parts of the protocore to enable the existence of iron melts and prohibit freezing within the iron-rich channels.

First, as a melt channel propagates away from source, iron melt flows through an increasingly wider channel because of the accumulation of melt and the possible drainage of the diapir thereby. A wider channel prolongs the cooling time. Secondly the release of potential energy due to the segregation of iron from the silicates is also a feasible mechanism. For iron which sinks to the centre of the Earth the following formulae from Schubert et al. (1986) are valid for the potential energy before (E_1) and after the iron segregation (E_2)

$$E_1 = -\frac{16}{15}\pi^2 G\rho_{\mathrm{PC}}^2 R^5 \tag{21}$$

$$E_2 = -\frac{16}{15}\pi^2 GR^5\left[\rho_{\mathrm{Si}}^2 + \frac{5}{2}\rho_{\mathrm{Si}}(\rho_{\mathrm{PC}} - \rho_{\mathrm{Si}}) + \left(\frac{3}{2}\rho_{\mathrm{Si}} - \rho_{\mathrm{Fe}}\right)\cdot(\rho_{\mathrm{Si}} - \rho_{\mathrm{Fe}})\cdot\left(\frac{\rho_{\mathrm{PC}} - \rho_{\mathrm{Si}}}{\rho_{\mathrm{Fe}} - \rho_{\mathrm{Si}}}\right)^{5/3}\right] \tag{22}$$

where G is the gravitational constant, ρ is the density and R is the radius of the protoearth.

We estimate a temperature increase of

$$\Delta T = \frac{E_1 - E_2}{c_p\cdot M} \tag{23}$$

where c_p is the heat capacity at constant pressure and M the mass of the accreting protoearth.

With the values given in Table 1 and if we expect melting near the surface for size and mass values ranging from about present-day Mars (Melosh, 1990) to Earth ($R_{\mathrm{Mars}} = 3.397\cdot10^6$ m, $M_{\mathrm{Mars}} = 6.42\cdot10^{23}$ kg; $R_{\mathrm{Earth}} = 6.371\cdot10^6$ m, $M_{\mathrm{Earth}} = 5.97\cdot10^{24}$ kg) (Lodders and Fegley, 1998), we obtain a temperature increase due to differentiation ranging from 309 K to 771 K. Samuel and Tackley (2008) showed that a significant part of this potential energy will be released in the vicinity of the sinking diapirs, so the temperature will be high enough to melt silicates. This ensures the existence of molten iron in a solid matrix in the vicinity of an iron diapir, allowing for the formation of melt channels. Thus we expect that these two effects together provide an effective 'anti-freeze' for the cascading mechanism.

4.4. Model restrictions and applicability to the protocore

The applicability of our numerical results to the real protoearth depends on the value of Rt for the protocore. The estimated values of several parameters vary or are uncertain by orders of magnitude and so does the Rt number. But we expect that in the protocore the melt retention number is sufficiently small (see also the discussion at the end of Section 4.1). This is assured because of the low viscosity of the molten iron material η_f of 10^{-3}–10^0 Pa s (Rubie et al., 2003), the negligible grain size growth in the colder central parts of the protocore and the high viscosity in the protocore ranging from 10^{18} Pa s up to values of about 10^{28} Pa s in the centre (Karato and Murthy, 1997a). These tend to decrease the Rt value. So we believe that our results cover the part of the Rt spectrum which is applicable in the protocore. Another shortcoming of our model is the use of a truncation porosity of $\phi = 0.2$ because of the restriction associated with the applied CBA approximation. Our results can strictly be applied to the real protoearth only during the early development of melt channelling. Thus the observed draining of melt by channelling represents only the upper bound for the time scale of melt channel formation.

Finally, one might also ask whether the melt channels might induce dykes instead of daughter diapirs, which could drain the region around the first diapir and then traverse to the centre of the protocore in a short time. Indeed, results by Rubin (1993a) indicate that when the viscosity contrast between fluid and host rocks is greater than 10^{11}–10^{14}, dykes can exist, but one has to keep in mind that the temperature profile for the early Earth – and also the composition and viscosity of protocore material in greater depths and under the conditions proposed here – are highly unknown. The absence of chondritic silicate+iron mixtures within the deep mantle of today's Earth could be an indication for effective draining of this region during the early history of the Earth. Another possible explanation of core formation without melt channelling would be the complete melting of this inner region of the accreting Earth and the separation using the 'rainfall' mechanism. We believe that it is possible that both mechanisms supplement each other in draining some regions. However, it has to be taken into account that very high energetic impacts are needed to melt the deeper parts of the protocore completely. So it is doubtful, whether terrestrial planets could ever have been completely molten (Stevenson, 1983). Thus, given the

uncertainties of the rheology under high pressure conditions within the protoearth, which have not been explored experimentally so far, a final decision between the mechanisms including the cascading diapirs and melt channelling and the dyke mechanism as a fast mechanism of core formation is not possible at the moment.

5. Conclusions

We propose the application of the melt channelling instability on the sinking of iron diapirs during Earth's core formation. Our results cover the range of diapir radii and melt retention values reasonable for the protoearth. They show that melt channels are generated in these cases and that mature channels are able to move the melt for retention numbers of 1.0 or less with at least a factor 1.2 to 1.6 higher velocities than the Stokes sinking velocity of a diapir. Furthermore, melt channelling and drainage increases the effective viscosity around the diapir and significantly slows down its sinking velocity. We propose the development of a cascading mechanism, which generates new melt diapirs from accumulated melt at the base of the high stress-vicinity of the mother diapir.

The formation of diapirs is possible due to the action of the power law under high pressure conditions, which reduces the viscosity of the surrounding medium in the protoearth. We show that if the mother diapir leaks through the channels, the new diapirs significantly increase in size, suggesting that they induce new melt channels in subsequently larger regions. Based on this concept we expect cone-like drainage regions extending with depth until, depending on the initial wavelength, these diapirs will start to interact and their draining zones will decrease. Furthermore, the mechanism is able to aid, together with the 'rainfall' mechanism, the drainage and segregation of the iron in the lower part of the protocore from the chondritic starting material of the solar system. Further improvements to the model should include stress-dependent viscosity and permeability and the introduction of a realistic depth-dependent temperature and viscosity profile.

Acknowledgements

We thank Kai Stemmer and an anonymous reviewer for their valuable suggestions. Nickolai Bagdassarov and Henri Samuel helped to improve the manuscript by helpful comments and discussions. GJG was supported by project ETH 0-20414-07.

Appendix A. Supplementary data

Supplementary data associated with this article can be found, in the online version, at doi:10.1016/j.epsl.2008.02.033.

References

Carlson, R.W., Lugmair, G.W., 2000. Timescales of planetesimal formation and differentiation based on extinct and extant radioisotopes. In: Canup, R.M., Righter, K. (Eds.), Origin of the Earth and Moon. Arizona University Press, pp. 25–44.

Chambers, J.E., 2004. Planetary accretion in the inner solar system. Earth Planet. Sci. Lett. 223, 241–252.

Dahl, T.W., 2005. Turbulent Mixing during Planet Accretion and Core Formation: Interpretation of the Hf/W Chronometer and Implications for the Age of the Moon. M. Sc. Thesis, University of Copenhagen.

Elsasser, W.M., 1963. Early history of the Earth. In: Geiss, J., Goldberg, E. (Eds.), Earth Science and Meteoritics. North-Holland, Amsterdam, pp. 1–30.

Höink, T., Schmalzl, J., Hansen, U., 2006. Dynamics of metal–silicate separation in a terrestrial magma ocean. Geochem. Geophys. Geosyst. 7. doi:10.1029/2006GC001268.

Honda, R., Mizutani, H., Yamamoto, T., 1993. Numerical simulation of Earth's core formation. J. Geophys. Res. 98, 2,075–2,089.

Hustoft, J.W., Kohlstedt, D.L., 2006. Metal–silicate segregation in deforming dunitic rocks. Geochem. Geophys. Geosyst. 7. doi:10.1029/2005GC001048.

Ghosh, A., McSween Jr., H.Y., 1998. A thermal model for the differentiation of Asteroid 4 Vesta. based on radiogenic heating. Icarus 134, 187–206.

Groebner, N., Kohlstedt, D.L., 2006. Deformation-induced metal melt networks in silicates, Implications for core–mantle interactions in planetary bodies. Earth Planet. Sci. Lett. 245, 571–580.

Kallemeyn, G.W., Rubin, A.E., Wang, D., Wasson, J.T., 1989. Ordinary chondrites: bulk composition, classification, lithophile-element fractionations and composition—petrographic type relationships. Geochim. Cosmochim. Acta 53, 2,747–2,767.

Karato, S.-i., Murthy, V.R., 1997a. Core formation and chemical equilibrium in the Earth I. Physical considerations. Phys. Earth Planet. Int. 100, 61–79.

Katz, R.F., Spiegelman, M., Holtzman, B., 2006. The dynamics of melt and shear localization in partially molten aggregates. Nature 442. doi:10.1038/nature05039.

Kohlstedt, D., Bai, Q., Wan, Z., Mei, S., 2000. Rheology of partially molten rocks. In: Bagdassarov, N., Laporte, D., Thompson, A.B. (Eds.), Physics and Chemistry of Partially Molten Rocks. Springer, New York, pp. 1–28.

Lin, J.R., Gerya, T.V., Tackley, P.J., Yuen, D.A., in preparation. Primordial Core Destabilization during Planetary Accretion: Influence from Deforming Planetary Surface.

Lodders, K., Fegley, B., 1998. The Planetary Scientist's Companion, First Ed. Oxford University Press, New York.

Melosh, H.J., 1990. Giant impacts and the thermal state of the early Earth. In: Newsom, H.E., Jones, J.H. (Eds.), Origin of the Earth. Oxford University Press, pp. 69–83.

Merk, R., Breuer, D., Spohn, T., 2002. Numerical modeling of ^{26}Al-induced radioactive melting of asteroids considering accretion. Icarus 159, 183–191.

McKenzie, D., 1984. The generation and compaction of partially molten rock. J. Petrol. 25, 713–765.

Müller, K., 2005. Numerische Untersuchung der spannungsgetriebenen Schmelzsegregation mit Anwendung auf einen Plume unter einem Mittel-Ozeanischen Rücken. PhD thesis, University of Frankfurt.

Müller, K., Schmeling, H., in review. Melt Segregation by Channelling within Partially Molten Rock under Large Shear Deformation. Geochem. Geophys. Geosyst.

Ricard, Y., Bercovici, D., Schubert, G., 2001. A two phase model for compaction and damage: 2: compaction. J. Geophys. Res. 106, 8,907–8,924.

Richardson, C.N., 1998. Melt flow in a variable viscosity matrix. Geophys. Res. Lett. 25, 1,099–1,102.

Rubie, D.C., Melosh, H.J., Reid, J.E., Liebske, C., Righter, K., 2003. Mechanisms of metal-silicate equilibration in the terrestrial magma ocean. Earth Planet. Sci. Lett. 205, 239–255.

Rubie, D.C., Nimmo, F., Melosh, H.J., 2007. Formation of the Earth's Core. In: Stevenson, D.J. (Ed.), Treatise on Geophysics. Evolution of the Earth, vol. 9. Elsevier B.V., Amsterdam, pp. 51–90.

Rubin, A.M., 1993a. Dikes vs. diapirs in viscoelastic rock. Earth Planet. Sci. Lett. 117, 653–670.

Rushmer, T., Minarik, W.G., Taylor, G.J., 2000. Physical processes of core formation. In: Canup, R.M., Righter, K. (Eds.), Origin of the Earth and Moon. Arizona University Press, pp. 227–245.

Samuel, H., Tackley, P.J., 2008. Dynamics of Core Formation and Equilibration by Negative Diapirism, Geochem. Geophys. Geosyst., in review.

Schmeling, H., 2000. Partial melting and melt segregation in a convecting mantle. In: Bagdassarov, N., Laporte, D., Thompson, A.B. (Eds.), Physics and Chemistry of Partially Molten Rocks. Springer, New York, pp. 141–178.

Schubert, G., Spohn, T., Reynolds, R.T., 1986. Thermal histories, compositions and internal structures of the moons of the solar system. In: Burns, J.A., Matthews, M.S. (Eds.), Satellites. Arizona University Press, pp. 224–292.

Solomatov, V.S., Stevenson, D.J., 1993c. Kinetics of crystal growth in a terrestrial magma ocean. J. Geophys. Res. 98, 5,407–5,418.

Steinberger, B., Calderwood, A.R., 2006. Models of large-scale viscous flow in the Earth's mantle with constraints from mineral physics and surface observations. Geophys. J. Int. 167, 1,461–1,481.

Stevenson, D.J., 1981. Models of the Earth's core. Science 214, 611–619.

Stevenson, D.J., 1983. The nature of the Earth prior to the oldest known rock record: The Hadean Earth. In: Schopf, J.W. (Ed.), Origin and Evolution of the Earth's Earliest Biosphere: An Interdisciplinary Study. Princeton University Press, pp. 32–40.

Stevenson, D.J., 1989. Spontaneous small-scale melt segregation in partial melts undergoing deformation. Geophys. Res. Lett. 16, 1,067–1,070.

Stevenson, D.J., 1990. Fluid dynamics of core formation. In: Newsom, H.E., Jones, J.H. (Eds.), Origin of the Earth. Oxford University Press, pp. 231–249.

Tackley, P.J., Stevenson, D.J., 1993. A mechanism for spontaneous self-perpetuating volcanism on the terrestrial planets. In: Stone, D.B., Runcorn, S.K. (Eds.), Flow and Creep in the Solar System: Observations, Modeling and Theory. Kluwer, Dordrecht, pp. 307–321.

Takafuji, N., Xu, G., Mitome, J., Bando, Y., Hirose, K., Ono, S., 2004. Segregation of core melts by permeable flow in the lower mantle. Earth Planet. Sci. Lett. 224, 249–257.

Taylor, S.R., Norman, M.D., 1990. Accretion of differentiated planetesimals to the Earth. In: Newsom, H.E., Jones, J.H. (Eds.), Origin of the Earth. Oxford University Press, pp. 29–43.

Terasaki, H., Frost, D.J., Rubie, D.C., Langenhorst, F., 2007b. The interconnectivity of Fe–O–S liquid in polycrystalline silicate perovskite at lower mantle conditions. Phys. Earth. Planet. Int. 161, 170–176.

Weinberg, R.F., Schmeling, H., 1992. Polydiapirs: multiwavelength gravity structures. J. Struct. Geol. 14, 425–436.

Wetherill, G.W., 1990. Formation of the Earth. Annu. Rev. Earth Planet. Sci. 18, 205–256.

Yoshino, T., Walter, M.J., Katsura, T., 2004. Connectivity of molten Fe alloy in peridotite based on in situ electrical conductivity measurements: Implications for core formation in terrestrial planets. Earth Planet. Sci. Lett. 222, 625–643.

Ziethe, R., Spohn, T., 2007. Two-dimensional Stokes flow around a heated cylinder: a possible application for diapirs in the mantle. J. Geophys. Res. 112, B09403. doi:10.1029/2006JB004789.

Ziethe, R., Nyffenegger, O., Benz, W., in preparation. A Consistent Model for the Accretion and Differentiation of Terrestrial Planets: Implications from the Combination of Monte-Carlo Models for Planet Formation and Finite Element Models for Core Formation.